Journal of Fluids and Structures 87 (2019) 137–149

Contents lists available at ScienceDirect

Journal of Fluids and Structures

journal homepage: www.elsevier.com/locate/jfs

Blade dynamics in combined waves and current

Jiarui Lei *, Heidi Nepf

Department of Civil and Environmental Engineering, Massachusetts Institute of Technology, Cambridge, MA, United States

HIGHLIGHTS

- A new prediction of drag on a flexible blade in combined wave and current is derived and validated with experiments.
- The drag on a flexible blade in waves decreases with increasing current magnitude.
- The limits of wave-dominated and current-dominated drag are defined.

ARTICLE INFO

Article history:
Received 25 September 2018
Received in revised form 15 March 2019
Accepted 19 March 2019
Available online 29 March 2019

Keywords:
Reconfiguration
Fluid–structure interaction
Combined wave–current
Flexible vegetation
Effective length

ABSTRACT

Submerged aquatic vegetation (SAV), such as seagrass, is flexible and reconfigures (bends) in response to waves and current. The blade motion and reconfiguration modify the hydrodynamic drag. The modified drag can be described by an effective blade length, l_e, which is defined as the length of a rigid blade that results in the same drag as a flexible blade of length l. In many natural settings SAV is exposed to combinations of waves and current. This study derived and used laboratory measurements to validate new predictions of effective blade length for combined waves and current based on a Cauchy number, which describes the ratio of hydrodynamic drag to the restoring force due to rigidity of blade. Force measurements on and digital images of blades exposed to waves with a 2-s period and with a range of wave velocity (U_w) and current speed (U_c) were used to estimate the effective blade length. The measurements were also used to validate a numerical simulation of blade motion. Once validated, the simulation was used to expand the investigated parameter space to a wider range of wave conditions, and in particular longer wave periods. For $U_c < \frac{1}{4}U_w$, the blade motion and hydrodynamic drag were wave-dominated. For $U_c > 2U_w$, the blade motion and hydrodynamic drag were current-dominated.

1. Introduction

Submerged aquatic vegetation (SAV) provides many ecosystem services (Barbier et al., 2011). They are important habitats and shelter areas for fish and shellfish, and supply food for herbivorous animals such as dugongs, manatees and sea turtles (Costanza et al., 1997; Waycott et al., 2005). Seagrass, a common marine SAV, is a significant global carbon sink, sequestering more carbon per hectare than rainforests (Fourqurean et al., 2012). Other studies have shown that SAV can protect shorelines from erosion by attenuating wave energy (e.g. Bradley and Houser, 2009; Infantes et al., 2012; Arkema et al., 2017). Understanding wave attenuation by SAV would be useful in predicting coastal protection provided by SAV and for understanding how SAV promotes particle retention and carbon sequestration.

* Corresponding author.
E-mail address: garylei@mit.edu (J. Lei).

https://doi.org/10.1016/j.jfluidstructs.2019.03.020

Many previous studies have characterized the damping of waves by vegetation, both using model vegetation in the lab (e.g. Mendez and Losada, 2004; Augustin et al., 2009; Stratigaki et al., 2011) and through field studies (e.g. Bradley and Houser, 2009; Paul and Amos, 2011; Infantes et al., 2012). Some of these studies have accounted for the flexibility of the vegetation. For example, Mullarney and Henderson (2010) developed an analytical model based on cantilever beam theory to simulate the movement of single-stemmed vegetation, such as sedges. The model predicted that wave damping by flexible vegetation was just 30% of that by rigid vegetation. Houser et al. (2015) investigated the dependence of the drag coefficient on blade flexibility, and, similar to Mullarney and Henderson (2010), they found that drag force was reduced with increasing blade flexibility.

In many natural settings, SAV is exposed to waves and current together (e.g. Ysebaert et al., 2011), but only a handful of studies have considered the impact of current on wave damping by vegetation. Li and Yan (2007) used a three-dimensional RANS model and Hu et al. (2015) used a laboratory study to show that current flowing in the direction of wave propagation enhances wave dissipation. However, both studies only considered rigid vegetation. Paul et al. (2012) conducted flume experiments with flexible model vegetation and observed the opposite trend, i.e. the presence of current reduced wave dissipation. Losada et al. (2016) performed laboratory experiments using real vegetation and found that wave damping was enhanced by current flowing in the opposite direction, but was reduced by current in the same direction as wave propagation. Losada et al. (2016) proposed a new description for wave damping that accounted for the blade deflection by the current. Specifically, in the description of wave energy dissipation the full blade length, l, was replaced by the measured deflected height, h_D, defined as the vertical distance between the time-mean position of the blade tip and the bed. This paper will build on the work of Losada et al. (2016), by providing a way to predict the deflected height, *a priori*, rather than relying on measured h_D. Further, this paper develops a model to predict the hydrodynamic drag on a single flexible blade interacting with combined waves and current by considering how flexible blades move in response to water motion. The new model can form the basis for predicting wave energy dissipation.

Luhar and Nepf (2011, 2016) defined an effective blade length, l_e, to characterize the impact of reconfiguration on the drag force on an individual blade in unidirectional flow and in waves. The effective length is defined as the length of a rigid blade that experiences the same drag as a flexible blade of length l. Generally, reconfiguration reduces drag, such that $l_e < l$. The reduction in drag is associated with the reduction in plant frontal area as well as the streamlining of the blade, and for wave conditions, the motion of the blade reduces the relative velocity between the blade and the water. The effective blade length provides a way to modify models that predict wave damping for rigid stems to predict wave damping by flexible stems. Dalrymple et al. (1984) derived a wave decay coefficient, K_D, for linear waves propagating over a meadow of vegetation consisting of an array of rigid blades of length l.

$$K_D = \frac{2}{9\pi} C_D a_v k \left(\frac{9\sinh(kl) + \sinh(3kl)}{\sinh kh(\sinh(2kh) + 2kh)} \right) \tag{1}$$

Here, a_v is the plant frontal area per meadow volume, k is the wave number and h is the water depth. Lei and Nepf (2019) demonstrated that Eq. (1) predicts wave decay over a flexible meadow, if l is replaced with l_e, with l_e described by scaling laws developed for individual blades in pure waves (Luhar and Nepf, 2016). The present paper builds on this concept by developing scaling laws for l_e that apply to conditions with combined waves and current. To facilitate the discussion, we review the scaling laws previously developed for blades in pure current and in pure waves in Section 2.

This study seeks to extend the concept of effective blade length to conditions with combined waves and current. First, building on existing scaling laws for pure current and pure waves (described below), a new scaling law is proposed for l_e/l under conditions with combined waves and current. Second, the new formulation is tested using measured and simulated drag forces on individual model blades. Finally, digital video images are used to examine the blade motion in greater detail to support the description of the scaling laws.

2. Scaling laws for blades in combined wave and current

The change in blade posture in response to water motion, called reconfiguration (Fig. 1), can be described by three dimensionless parameters (e.g. Luhar and Nepf, 2011, 2016). First, the Cauchy number, shown in Eq. (2), is the ratio of hydrodynamic drag to the restoring force due to blade stiffness. As shown in Eq. (2), the Cauchy number has a different definition in pure current (U_c), denoted Ca_c, and in pure waves (U_w), denoted Ca_w. Second, the buoyancy parameter, B, is the ratio between restoring forces due to buoyancy and to blade stiffness. Third, the blade length ratio, L, is the ratio of blade length, l, to wave excursion, A_w $(= U_w T/2\pi)$, which is the radius of the wave orbital (Fig. 1), with T the wave period.

$$Ca_c = \frac{\frac{1}{2} C_D \rho b U_c^2 l^3}{EI} \qquad Ca_w = \frac{\frac{1}{2} C_D \rho b U_w^2 l^3}{EI} \tag{2}$$

$$B = \frac{\Delta\rho g b d l^3}{EI} \tag{3}$$

$$L = \frac{l}{A_w} = \frac{2\pi l}{U_w T} \tag{4}$$

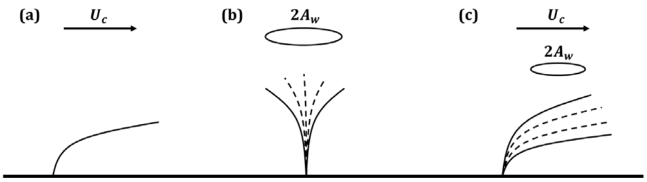

Fig. 1. Blade reconfiguration in (a) pure current, (b) pure waves, and (c) combined waves and current. Solid lines denote the maximum pronation. Dashed lines indicate the range of blade position over the wave cycle. The wave orbital diameter, which is equal to twice the wave excursion, $2A_w$, is shown in (b) (c).

Here, C_D is the drag coefficient for a vertical, rigid blade, which, as discussed below, is a function of the flow velocity. Further, b and d are the blade width and thickness, respectively, ρ is the density of water, $\Delta\rho$ is the difference in density between the water and the blade, E is the Young's modulus, and $I = \frac{bd^3}{12}$ is the bending moment of inertia. Note that previous papers excluded the term $\frac{1}{2}C_D$ in the definition of wave Cauchy number, Ca_w (Luhar and Nepf, 2016; Luhar et al., 2017). However, to facilitate the combination of waves and current, in this paper it is convenient to have identical forms for Ca_c and Ca_w (as in Eq. (2)).

For unidirectional current, the balance of hydrodynamic drag ($\frac{1}{2}C_D\rho b l_e U_c^2$) to blade restoring force ($-EI\frac{\partial^2\theta}{\partial s^2} \sim -EI\frac{1}{l_e^2}$, with s the distance along the blade) yields the following scaling law (e.g. Alben et al., 2002; Gosselin et al., 2010).

$$\frac{l_e}{l} \sim Ca_c^{-1/3} \tag{5}$$

Luhar and Nepf (2011) additionally considered the role of buoyancy, described by the buoyancy parameter, B, defined in Eq. (3). A combination of physical experiment and numerical modeling was used to develop the following predictor for effective blade length with current only,

$$\frac{l_e}{l} = 1 - \frac{1 - 0.9Ca_c^{-1/3}}{1 + Ca_c^{-\frac{3}{2}}(8 + B^{\frac{3}{2}})} \tag{6}$$

As described in Luhar and Nepf (2011), Eq. (6) captures two limits of reconfiguration. First, if the drag force is too small to overcome blade buoyancy ($\frac{Ca_c}{B} < 1$) and blade rigidity ($Ca_c < 1$), no reconfiguration occurs and Eq. (6) reduces to $l_e/l \approx 1$. In this case, the blade behaves as if it were rigid. Second, when the hydrodynamic drag force is larger than both buoyancy ($Ca_c \gg B$) and rigidity ($Ca_c \gg 1$), Eq. (6) reduces to

$$\frac{l_e}{l} = 0.9Ca_c^{-1/3}, \tag{7}$$

which is the same scaling law presented in Eq. (5) and described in Alben et al. (2002). As shown in Table 2 of Lei and Nepf (2016), for many species of SAV, B is in the range 0 to 1.4. In addition, for a wide range of field conditions, $Ca_c \gg 1$, indicating that the blade buoyancy is not dynamically significant for most SAV except at the limit of quiescent conditions (no waves and no current), such that Eq. (7) describes most blade behavior. Based on this, and to simplify the study presented here, the impact of B on blade motion and effective length is neglected, and Eq. (7) is used as the current-only scaling law.

For waves with no current there are three regimes of blade motion. If the wave drag is insufficient to overcome the blade rigidity ($Ca_w < 1$), the blade does not reconfigure and behaves as a rigid blade, such that $l_e/l = 1$. If the wave drag is sufficient to bend the blade, two regimes of behavior exist. First, if the blade length (l) is comparable to or greater than the wave excursion ($A_w = U_w T/2\pi$, with $2A_w$ the wave orbital diameter shown in Fig. 1), i.e. $L \geq 1$, the upper part of the blade can follow the fluid motion over the wave cycle. The blade tip excursion approximates the wave excursion, such that the maximum blade bending angle $\theta \sim A_w/l_e$ (Luhar and Nepf, 2016). In this case, the blade rigidity exerts a restoring force proportional to $EI\frac{\partial^2\theta}{\partial s^2} \sim EI\frac{A_w}{l_e^3}$, which balances the drag force ($\sim C_D\rho b l_e U_w^2$), yielding the following theoretical scaling law.

$$\frac{l_e}{l} \sim (Ca_w L)^{-1/4} \quad (L \geq 1) \tag{8}$$

Eq. (8) was confirmed for individual flexible blades. Specifically, using drag measured on individual model blades and the Cauchy number $Ca_{wLN} = \rho b U_w^2 l^3/EI$, Lei and Nepf (2019) showed that $l_e/l = (0.94 \pm 0.06)(Ca_{wLN}L)^{-0.25\pm0.02}$. Note that Ca_{wLN} differs from the definition used in Eq. (2) by the factor $\frac{1}{2}C_D$. Using the Lei and Nepf (2019) data set, but with the Cauchy number (Ca_w) defined in Eq. (1),

$$\frac{l_e}{l} = (1.09 \pm 0.07)(Ca_w L)^{-0.25\pm0.02} \quad (L \geq 1,\ \text{short waves}) \tag{9}$$

In the second wave regime the blade length is much less than the wave orbital excursion ($L \ll 1$), and the blade only moves during part of a wave cycle and remains essentially stationary at its maximum pronation during the rest of the cycle (Fig. 1), as described in Zeller et al. (2014) and in the large amplitude regime of Leclercq and de Langre (2018). Luhar and Nepf (2016) hypothesized that if the blade is stationary during the majority of the wave cycle, the effective length can be described by the scaling for current (Eq. (7)), but using the wave velocity as the relevant velocity scale, i.e. replacing U_c by U_w. This assumes that the scaling depends on the peak drag. Alternatively, we suggest here that the scaling depends on the equivalent mean drag over the wave period, which requires $\frac{1}{2}C_D\rho bl_e\left(\frac{1}{2}U_w^2\right) = \frac{1}{2}C_D\rho bl_e U_c^2$, suggesting that the appropriate equivalence is $Ca_c = \frac{1}{2}Ca_w$. Making this substitution in Eq. (7),

$$\frac{l_e}{l} = 0.9\left(\frac{1}{2}Ca_w\right)^{-1/3} = 1.1Ca_w^{-1/3} \quad (L \ll 1, \text{long waves}) \tag{10}$$

Finally, we consider a combined wave–current flow, with total flow velocity $U(t) = U_w \sin(2\pi t/T) + U_c$. The drag force on an individual rigid blade of length l is proportional to ρblU^2. Using the combined wave–current velocity, U, and integrating the drag magnitude over the wave period, the mean drag magnitude on a vertical, rigid blade is

$$F_{mean,rigid} = \frac{1}{2}\rho C_D bl\left(U_c^2 + \frac{1}{2}U_w^2\right). \tag{11}$$

This suggests that the time-mean, absolute drag on a rigid blade in combined wave and current is equivalent to the mean drag imposed by a unidirectional current of magnitude $(U_c^2 + \frac{1}{2}U_w^2)^{1/2}$. Based on this, we hypothesized that the effective blade length, specifically l_e/l, in combined wave–current may be described by a modified version of the unidirectional current model (Eq. (7)), replacing the current Cauchy number (Ca_c) with a new Cauchy number defined for combined wave and current (Ca_{wc}) that uses the equivalent current defined above, i.e.

$$Ca_{wc} = \frac{1}{2}\frac{C_D\rho bl^3}{EI}\left(U_c^2 + \frac{1}{2}U_w^2\right), \tag{12}$$

and

$$\frac{l_e}{l} = 0.9Ca_{wc}^{-1/3} \tag{13}$$

When the wave velocity magnitude, U_w, is small compared to the current, U_c, Eq. (13) reverts to Eq. (7). However, when $U_c < U_w$, the effective length ratio is expected to revert back to the wave-only scaling law, given in Eq. (9). The transition to the current-dominated (Eq. (7)) and wave-dominated (Eq. (9)) limits can be predicted by considering the time-varying drag on a rigid blade,

$$F_{cw,rigid}(t) = \frac{1}{2}\rho C_D bl\left(\left(U_c^2 + \frac{1}{2}U_w^2\right) + 2U_cU_w \sin\left(\frac{2\pi t}{T}\right) - \frac{1}{2}U_w^2 \cos\left(\frac{4\pi t}{T}\right)\right) \tag{14}$$

The first term on the RHS is the time-mean absolute drag force (as in Eq. (10)), and the next two terms are the oscillating components of drag force. The added mass will be shown to be small (see discussion after Eq. (27)), and is excluded here for simplicity. The current contribution to drag will dominate, and Eq. (7) should predict l_e/l, when the oscillating component of drag is small compared to the mean. The maximum of the oscillating component of drag is

$$max\left(2U_cU_w \sin\left(\frac{2\pi t}{T}\right) - \frac{1}{2}U_w^2 \cos\left(\frac{4\pi t}{T}\right)\right) = 2U_cU_w + \frac{1}{2}U_w^2, \tag{15}$$

so that the oscillating component of drag is small compared to the mean drag when

$$2U_cU_w + \frac{1}{2}U_w^2 < \left(U_c^2 + \frac{1}{2}U_w^2\right), \tag{16}$$

or

$$U_c > 2U_w \qquad \text{current-dominated drag} \tag{17}$$

Eq. (17) defines the limit for current-dominated drag. In contrast, the wave contribution to drag will dominate, and Eq. (9) should predict l_e/l when both

$$\begin{gathered} U_c^2 < \frac{1}{2}U_w^2 \\ \text{and} \quad \left|2U_cU_w \sin\left(\frac{2\pi t}{T}\right)\right| < \left|\frac{1}{2}U_w^2 \cos\left(\frac{4\pi t}{T}\right)\right| \end{gathered} \tag{18}$$

To satisfy both conditions,

$$U_c < \frac{1}{4}U_w \qquad \text{wave-dominated drag} \tag{19}$$

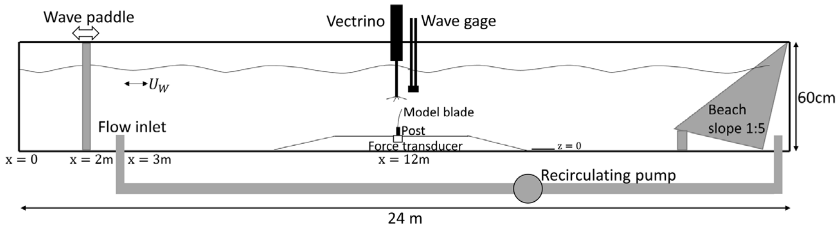

Fig. 2. Experimental set up to measure drag on individual model blades (not to scale). The force transducer was housed within an acrylic box with tapered ends. Water depth over the ramp was 28 cm. The velocity was measured with a Nortek Vectrino placed directly above the blade post, but without a model blade. The water surface displacement was measured with a wave gage positioned laterally adjacent to the Vectrino.

In between the limits defined by Eqs. (17) and (19), i.e. $\frac{1}{4} < U_c/U_w < 2$, both waves and current contribute significantly to blade drag, and we propose that Eq. (13) will predict l_e/l. These hypotheses will be tested using a combination of laboratory experiment and numerical simulation.

3. Laboratory experiments

Laboratory experiments were carried out in a 24 m long and 38 cm wide water channel (Fig. 2). A single model blade was attached to a 4 cm long, 2 mm wide stainless steel post, which was attached to a submersible force transducer (Futek LSB210). The force transducer was mounted beneath a 12 cm high, 2 m long acrylic ramp that spanned the channel width. The horizontal top of the ramp was 1 m long. The ramp was placed 9 m downstream from the channel inlet. The force transducer had a resolution of 0.0001 N and was calibrated by National Instrument (NI). The channel was filled to 40 cm total depth, such that the water depth above the ramp was 28 cm. A wave gage was mounted above the ramp at mid-length along the ramp and 5 cm away from the sidewall (laterally 14 cm away from the blade post). The horizontal force and the water surface displacement were synchronized and logged using LabVIEW.

The model flexible blades were constructed from LDPE (low density polyethylene) film, which had a density of 0.92 g/cm^3 and a Young's modulus of 0.3 GPa. Three blade lengths, 5 cm, 10 cm and 15 cm, were cut from LDPE of two thicknesses, $d = 100$ μm and 250 μm. All blades had a width of $b = 1$ cm. The model rigid blades were constructed from 1.5 mm thick acrylic plates, to ensure sufficient rigidity. Blade length and width were the same as the flexible blades. Since drag depends on blade length and width but not thickness, and $d \ll b$, the greater thickness of the rigid blades should not significantly alter the drag.

Current was generated by a variable speed pump. Waves were generated by a programmable wavemaker. To reduce wave reflection, a 50 cm tall beach with 1:5 slope and covered with 10 cm of coconut fiber was placed at the end of the flume. Using the method in Goda and Suzuki (1977), the wave reflection was evaluated as the amplitude ratio of incident wave to reflected wave and found to be less than 6% under pure waves and combined wave–current conditions. The beach toe was lifted 9 cm above the bed to allow the current to pass to the outlet. The current flowed in the direction of wave propagation with magnitudes of $U_c = 0$ to 12 cm/s. Two waves were considered, with wave velocity $U_w = 7.8$ cm/s and 11.0 cm/s, and both with a 2 s wave period. By varying the wave and current velocity, a wide range of the non-dimensional parameters was produced. Specifically, $Ca_c = 30$ to 860, $Ca_w = 0$ to 830, and $L = 1.4$ to 6.1. These values include reported field conditions. For example, as reported in Table 2 of Lei and Nepf (2016), field conditions for several SAV species correspond to $Ca_c = 0.04$ to 80,000. Similarly, under pure waves and for a typical range of $U_w = 0.05$ to 1 m/s and wave periods of $T = 1$ to 8 s (Bradley and Houser, 2009; Luhar and Nepf, 2013), the wave Cauchy number and the blade length ratio range between $Ca_w = 25$ to 2×10^6 and $L = 0.1$ to 75.

A 3-D Nortek Vectrino Acoustic Doppler Velocimeter (ADV) was used to measure velocity at individual points. To generate a vertical profile, the Vectrino was traversed vertically at 1 cm intervals from the ramp surface to 19 cm above the ramp. At each vertical position the velocity was measured for 2 min at a sampling rate of 200 Hz. The following procedure was used to find the time-mean (U_c) and phase-average wave velocity. Each velocity record was separated into 200T phase bins. To obtain accurate phase-averaged forces, the exact wave period was calculated using the MATLAB cross-correlation function ***xcorr***. By calculating the cross-correlation of the velocity to itself, ***xcorr***(U, U), the number of data points ($n_{onecycle}$) in each wave period was precisely defined. Specifically, $n_{onecycle} = 403$, which indicated the exact wave period to be $T = 403/200 = 2.015$ s, and the number of bins within one wave cycle was chosen to be $\gamma = 403$. The phase-average velocity in the nth phase bin ($n = 1$ to 403), which has wave phase $\phi = 2\pi n/\gamma$ is

$$\tilde{U}\,(\phi(n)) = \tilde{U}\left(\frac{2\pi n}{\gamma}\right) = \frac{1}{N}\sum_{m=0}^{N-1} U((n+\gamma m)) \tag{20}$$

in which $\tilde{U}$ denotes the phase-averaged velocity, N is the number of wave periods in the record, and $U((n+\gamma m))$ is the $(n+\gamma m)$th velocity sample. The current (U_c) and wave velocity magnitude (U_w) were calculated from the phase average

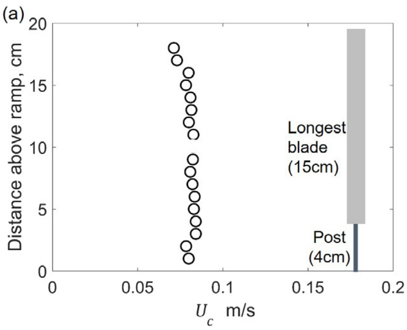

Fig. 3. Vertical profiles of (a) current velocity, U_c, and (b) wave velocity, U_w, measured above the ramp under a combined wave–current flow. The ramp surface is at z = 0. In (b), the solid line shows the wave velocity based on linear wave theory using the measured period ($T = 2.015$ s) and measured wave amplitude ($a_w = 2.0$ cm). The data points at 10 cm above the ramp are not shown, because this is the weak spot of the Vectrino. The uncertainty in the velocity measurements is smaller than the symbol. Cartoons of the post and blade are shown within each subplot to illustrate the maximum possible vertical extent within which the blade was located while moving and reconfiguring under the waves and current. To see real blade motion, refer to Fig. 6. The degree of vertical uniformity in U_c and U_w was similar across the entire range of flow conditions (data not shown).

velocity as,

$$U_c = \frac{1}{2\pi}\int_0^{2\pi} \tilde{U}(\phi)\, d\phi \tag{21}$$

and

$$U_w = \sqrt{2}\ \mathrm{RMS}\left(\tilde{U}(\phi) - U_c\right) = \sqrt{2}\sqrt{\frac{1}{2\pi}\int_0^{2\pi} (\tilde{U}(\phi) - U_c)^2 d\phi} \tag{22}$$

Over the ramp, where the blades were deployed, the current velocity was close to uniform over depth, with a narrow boundary layer (e.g. Fig. 3a). Similarly, the wave velocity was also nearly uniform over depth (e.g. Fig. 3b). The measured wave velocity agreed with linear wave theory with a maximum difference of 7% (Fig. 3b). With the blade mounted on the post, the blade position in the water column varied with the wave and current conditions, but was always between 4 and 19 cm above the ramp, a region within which the time-mean and wave velocity were close to uniform. The measured surface displacement, $\eta(t)$, was used to estimate the wave amplitude a_w as the root-mean-square surface displacement, $a_w = \sqrt{2}\mathrm{RMS}(\eta(t))$.

For each wave–current combination, the drag force was measured at 1200 Hz for three minutes, which represented about 90 waves. A FFT (fast Fourier transform) in MATLAB was used to filter out high-frequency noise. The filtered force record, $F(t)$, was separated into 1200 T phase bins to find the phase-averaged force. The number of force measurements per wave cycle was $\gamma = 2418$. Using a phase-averaging method similar to that applied to the velocity record, the phase-average drag force on the blade and post together, referred to as the total force, was calculated as,

$$\tilde{F}_{total}(\phi(n)) = \frac{1}{N}\sum_{m=0}^{N-1} F(n + \gamma m), \tag{23}$$

The force on the post alone was also measured at each flow condition to define the phase-average force on the post $\tilde{F}_{post}(\phi)$. Fig. 4(a) shows an example of the phase-average drag forces on the post alone (red curve) and for the post and blade together (black curve). The surface displacement was measured synchronously with the force, and the phase-average surface displacement was similarly calculated (Fig. 4b). The standard deviation in the phase-average surface displacement was negligible ($<$ 2%), indicating that the individual waves were consistent through the time period. For convenience, zero phase was assigned at the crest.

The effective blade length ratio, l_e/l, was estimated as the ratio of measured time-mean absolute force on a flexible blade of length l (F_{mean}) to the measured time-mean absolute force on a rigid blade of length l ($F_{mean,rigid}$). For both rigid and flexible blades, the mean measured drag was estimated as the phase-average of the difference between the total force (post + blade) and the force on the post alone. For example, for flexible blades,

$$F_{mean} = \frac{1}{2\pi}\int_0^{\phi} |\tilde{F}_{total} - \tilde{F}_{post}|\, d\phi, \tag{24}$$

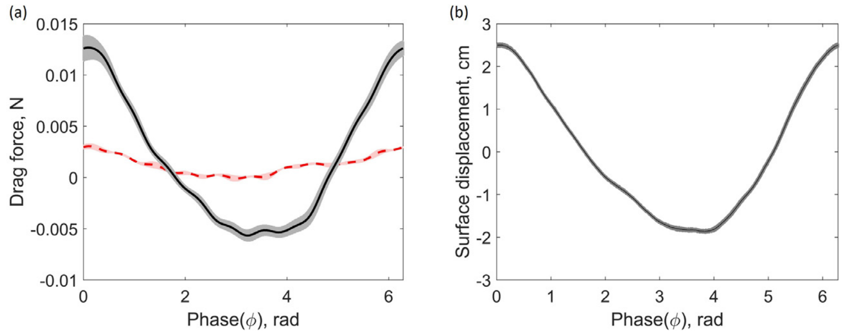

Fig. 4. (a) Phase-average force on a blade and post together, $\tilde{F}_{total}$, shown with black curve, and on the post alone, $\tilde{F}_{post}$, shown with red curve, plotted against wave phase ϕ. The shaded gray and red regions denote the uncertainty in $\tilde{F}_{total}$ and $\tilde{F}_{post}$, respectively, which was estimated as the standard deviation of all measurements within the phase bin. (b) Phase-average wave amplitude. The thin shaded gray region denotes the uncertainty in η, which was negligible. In this case, $U_w = 11.0$ cm/s and $U_c = 4.0$ cm/s. The blade was 10 cm long, 1 cm wide and 250 μm thick. (For interpretation of the references to color in this figure legend, the reader is referred to the web version of this article.)

and similarly for rigid blades. In Fig. 4 $F_{mean} = 0.0047 \pm 0.0006$ N. The measured effective length ratio was defined as the ratio of F_{mean} and $F_{mean,rigid}$.

$$\frac{l_e}{l}\,(measured) = \frac{F_{mean}}{F_{mean,rigid}} \tag{25}$$

The uncertainty in measured forces F_{mean} and $F_{mean,rigid}$ (shown in Fig. 4a) was propagated using standard methods to find the uncertainty in l_e/l (Taylor, 1997).

It is important to note that the estimation of the measured effective length, i.e. $\frac{l_e}{l}$ $(measured)$, was based only on measured forces and did not require an estimation of the drag coefficient, C_D. However, values of C_D for rigid blades were needed to estimate the Cauchy numbers and test the predictive scale equations. The drag coefficient in pure waves, $C_{D,w}$, depends on the Keulegan–Carpenter number, $KC = U_w T/b$. Based on measurements in Keulegan and Carpenter (1958), Luhar and Nepf (2016) suggested a wave drag coefficient for a rigid, flat plate,

$$C_{D,w} = \max(10KC^{-\frac{1}{3}}, 1.95) \tag{26}$$

In steady flow, the flat plate drag coefficient is $C_{D,c} = 1.95 + \frac{50}{Re}$, with Reynolds number $Re = U_c b/\upsilon$ (Ellington, 1991). To be consistent with the modified Cauchy number (Eq. (12)), in combined wave–current conditions we assumed a modified Reynolds number $Re = \left(U_c^2 + \frac{1}{2}U_w^2\right)^{1/2} b/\upsilon$. Then, for all conditions considered in this study, $Re > 550$, and $C_{D,c} = 1.95 + \frac{50}{Re} \approx 2$. However, Chandler and Hinwood (1982) show that when $0 \le \frac{U_c}{U_w} \le 1.2$, the ratio of drag coefficient in combined wave–current to pure waves $\frac{C_{D,wc}}{C_{D,w}}$ was in the range of 0.7 to 1.1. Following this, we assumed that the drag coefficient in combined wave–current flows was similar to that in pure waves, $C_{D,wc} = C_{D,w} = 4.0$ and 3.6 for $U_w = 11.0$ cm/s and 7.8 cm/s, respectively, based on Eq. (26).

The assumption that $C_{D,wc} = C_{D,w}$ was confirmed using force measurements on the rigid model blades. The drag coefficients were estimated in the following way. The drag force on a rigid blade can be described by the Morison equation (e.g. Luhar and Nepf, 2016), which results in the following time-average of absolute drag

$$F_{mean,rigid} = \frac{1}{T}\int_0^T \left| \int_0^l \frac{1}{2}\rho C_{D,wc} b\,|U|\,U + \rho\left(\frac{1}{4}b^2 C_M + bd\right)\frac{\partial U}{\partial t} \right| dzdt \tag{27}$$

Recall, $U(t)$ is the horizontal velocity in a combined wave–current flow. The drag coefficient in Eq. (27) corresponds to $C_{D,wc}$. For each wave–current condition, the velocity measured 6.5 cm above the ramp was used to represent the velocity over depth. As shown in Fig. 3, the wave and current velocity were uniform over the region occupied by the blades. Further, since the horizontal extent of the rigid vertical blade (i.e. the blade thickness) was much smaller than the wavelength (3.1 m), the streamwise variation in wave velocity can be neglected. The first term in Eq. (27) is the drag force and the second term is the added mass and the blade inertia, with C_M the added-mass coefficient. Since $d \ll b$, the blade inertia term was negligible relative to the added mass term. To compare drag and added mass we use representative values of $C_D = C_{D,w} = 4$, $C_M = 1$ and $U = \sqrt{U_c^2 + \frac{1}{2}U_w^2}$, based on values reported in Keulegan and Carpenter (1958). Using these values, the ratio of drag to added mass is $\frac{2TC_D U}{bC_M}$ ranged from 90 to 200, and clearly $\gg 1$, showing that the added mass term can be neglected. With these simplifications (i.e. neglecting both added mass and blade inertia), Eq. (27) becomes

$$F_{mean,rigid} = \frac{1}{T}\int_0^T |\frac{1}{2}\rho C_{D,wc} b\,|U|\,U|ldt = \frac{1}{2\pi}\int_0^{2\pi} |\frac{1}{2}\rho C_{D,w} b\left|\tilde{U}(\phi)\right|\tilde{U}(\phi)\,|ld\phi \tag{28}$$

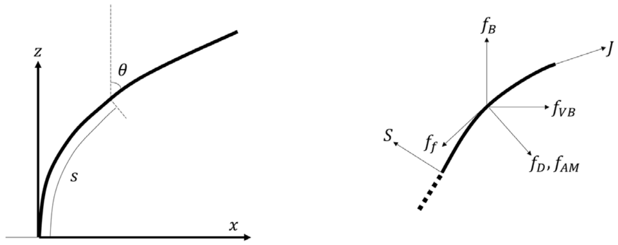

Fig. 5. Schematic of the force balance in Eq. (28).

Using the measured force on rigid blades $F_{mean,rigid}$ and the phase-average velocity $\tilde{U}(\phi)$, we obtained estimated values of drag coefficient in combined wave–current conditions, $C_{D,wc}$.

Finally, the blade motion was captured using a Canon 5D Mark III camera, which was mounted on a tripod looking through the side of the flume. Video was taken for 1 min (30 wave periods). The frame was 1280 × 720 pixels with an approximate field of view equal to 40 cm × 23 cm, and the frame rate was 50 fps. Using MATLAB, each video frame was converted to a black and white image, and edge detection was used to isolate the blade from the background. Finally, the images were stacked to show the range of motion during one wave period. The images were used to validate the numerical model described in the next section.

4. Numerical simulation

Luhar and Nepf (2016) developed a numerical model to simulate blade motion in waves. The MATLAB code can be found in Appendix C in Luhar (2012). The following balance of forces describes the blade motion. A schematic is shown in Fig. 5 to describe the force balance. Note that x and z are the streamwise and vertical coordinate directions; s is the distance along the blade from the bed; and θ is the angle between the blade and the vertical direction.

$$\frac{\partial}{\partial s}\left((S+iJ)\,e^{-i\theta}\right)+if_B+(f_D+if_F+f_{AM})\,e^{-i\theta}+f_{VB}=\rho_v bd\frac{\partial^2 x}{\partial t^2} \tag{29}$$

Here, $S = -\frac{\partial}{\partial s}(EI\frac{\partial\theta}{\partial s})$ is the restoring force due to blade rigidity; J is the tension in the blade; $f_B = \Delta\rho gbd$ is the buoyancy force; $f_D = \frac{1}{2}\rho C_D b\,|u_R|\,u_R$ is the drag force, with u_R the relative velocity between the fluid and the blade; $f_F = \frac{1}{2}\rho C_f b\,|u_R|\,u_R$ is the skin friction, with C_f the skin friction coefficient; $f_{AM} = \frac{\pi}{4}\rho C_M b^2(\left|\frac{\partial u_R}{\partial t}\right| e^{-i\theta})$ is the force due to added mass; $f_{VB} = \rho bd\frac{\partial u}{\partial t}$ is the virtual buoyancy force; and finally $\rho_v bd\frac{\partial^2 x}{\partial t^2}$ is the blade inertia.

Linear wave theory was used to create the velocity field within the simulation, because experimental measurements confirmed that this was a good representation of the conditions in the water channel (Fig. 3b). Because the blade length (5 cm, 10 cm or 15 cm) was much smaller than the wavelength (3.1 m), horizontal variation in velocity was neglected, and the simulation was set-up using the following velocity field.

$$U = U_c + \frac{\omega a_w}{\sinh kh}\cosh k(h+z)\sin(\omega t) \tag{30}$$

$$V = \frac{\omega a_w}{\sinh kh}\sinh k(h+z)\cos(\omega t) \tag{31}$$

Here, $\omega = 2\pi/T$ is the radian wave frequency, and k is the wavenumber. The simulation was validated by comparison to measured conditions using measured a_w, T and U_c in Eqs. (30) and (31). After validation, the simulation was run to explore a wider range of cases by choosing different values of a_w and U_c.

The simulation used Fornberg's (1998) algorithm to determine the weights in the finite difference formula. Eq. (29) is discretized in space with a central finite difference scheme with second-order accuracy. A forward Euler method with first-order accuracy was used in time. The boundary conditions were a fixed end at the blade base and a free end at the blade tip. Initially, the blade was upright. The simulation was run for 10 wave periods, within which the blade motion reached a quasi-steady state, i.e. with a repeatable sequence of posture and drag over the wave period. The simulation was used to estimate $F_{mean}(simulated)$, the mean absolute horizontal drag force on both flexible and rigid blades. The simulated effective length ratio was calculated based on Eq. (25), $\frac{l_e}{l}\,(simulated) = \frac{F_{mean}(simulated)}{F_{mean,rigid}(simulated)}$. Additional details and the validation of the numerical model is described in the supporting information.

5. Results/discussion

5.1. Blade imaging

Fig. 6 shows the motion of an individual blade over one wave period, comparing digital images and simulated motion. The wave condition was held constant across scenarios ($T = 2$ s, $U_w = 7.8$ cm/s), and the current increased in six

Fig. 6. Blade motion over one wave cycle based on digital images of real blades (top row) and numerical simulation (bottom row). For all images, $l = 10$ cm, $d = 100$ μm, $T = 2$ s, $U_w = 7.8$ cm/s, $Ca_w = 252$ and $L = 4.0$. Current increased from left to right (0, 2.0, 4.0, 6.0, 8.0, 10.0 cm/s), with $0 \leq Ca_c \leq 800$.

increments between $U_c = 0$ and 10 cm/s (left to right in figure). Blade motion in the zero-current case was similar to that in the convective regime in Leclercq and de Langre (2018). In this regime, the blade moved completely passively with the fluid particles over most of the blade length and most of the wave cycle. As the current increased, the mean pronation of the blade increased and the range of blade motion decreased. The simulated blade motion was qualitatively similar to the observed motion (Fig. 6).

The mean deflected height, h_d, was defined as the vertical distance between the time-mean position of the blade tip and the bed. The mean deflected height decreased with increasing current magnitude (Fig. 7). Luhar and Nepf (2013) provide an empirical equation for deflected height in unidirectional currents without waves (Eq. (4) in Luhar and Nepf, 2013, but repeated here).

$$\frac{h_d}{l} = 1 - \frac{1 - Ca^{-1/4}}{1 + Ca^{-\frac{3}{5}}\left(4 + B^{\frac{3}{5}}\right) + Ca^{-2}(8 + B^2)} \tag{32}$$

This equation is plotted as a solid curve in Fig. 7 using the current-only Cauchy number i.e. $Ca = Ca_c$ (Eq. (1)). The deflected height predicted from Eq. (32) agreed with measured values within uncertainty. This indicated that the time-mean pronation was dependent only on the time-mean velocity (current), even when the wave velocity ($U_w = 7.8$ cm/s) was comparable to and even larger than the current velocity ($U_c = 2$ to 10 cm/s). Finally, the simulated values of h_d (squares in Fig. 7) had reasonable agreement with the measured values (circles in Fig. 7), except for $Ca_{wc} = 380$ and 540, for which the simulation under-predicted the measured h_d by 21% and 24%, respectively (Fig. 7).

5.2. Measured forces on model rigid and flexible blades

The assumption that $C_{D,wc} = C_{D,w}$ was validated by using measured forces on rigid blades to estimate the drag coefficient in combined wave–current conditions. For $U_w = 7.8$ cm/s, and across all current speeds, the measured $C_{D,wc} = 3.7 \pm 0.7$, which agreed with the wave only value predicted from Eq. (26), $C_{D,w} = 4.0$. Similarly, for $U_w = 11.0$ cm/s, the measured value $C_{D,wc} = 3.1 \pm 0.6$, agreed with the predicted value $C_{D,w} = 3.6$. Further, the ratio of drag coefficient in combined wave–current to pure waves $C_{D,wc}/C_{D,w} = 0.93 \pm 0.18$ and 0.86 ± 0.17, for $U_w = 7.8$ and 11 cm/s, respectively, agreed with Chandler and Hinwood's (1982) observation that for $0 \leq \frac{U_c}{U_w} \leq 1.2$, the ratio $C_{D,wc}/C_{D,w}$ is in the range 0.7 to 1.1. In conclusion, for rigid blades, the assumption $C_{D,wc} = C_{D,w}$ was reasonable.

Based only on the measured forces on flexible and rigid blades, we calculated the measured effective length ratio using Eq. (25), $l_e/l\,(measured) = \frac{F_{mean}}{F_{mean,rigid}}$. Experimental results were shown in Table 1. In the supporting information (Fig. S3), we also compared the measured l_e/l with the simulated l_e/l, which confirmed that the simulation recreated the measured values.

5.3. Effective blade length behavior for combined wave and current

Measured and simulated values of effective blade length were used together to test the proposed wave–current model for effective blade length (Eq. (13)), as well as the hypothesized thresholds for current-dominated ($U_c > 2U_w$) and wave-dominated ($U_c < \frac{1}{4}U_w$) drag conditions. Fig. 8 compares the measured (circles) and simulated (crosses) effective blade lengths with the scaling equations shown with solid curves. The four sub-plots represent different combinations of blade

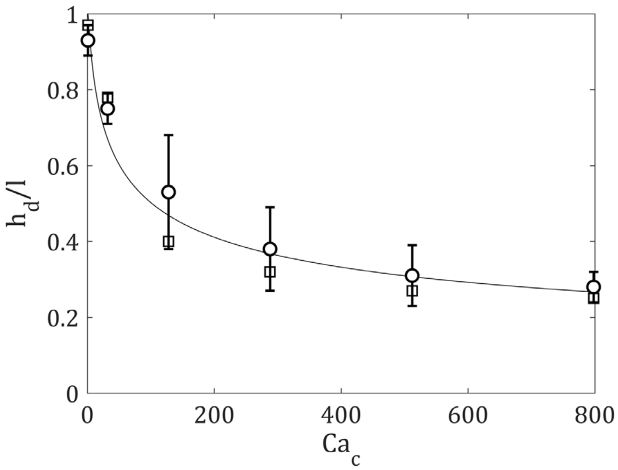

Fig. 7. Mean deflected height, h_d, from digital images (circles) and numerical simulation (squares). Black solid line denotes Eq. (32) evaluated using the current-only Cauchy number, Ca_c. Error bars indicate the 95% confidence interval for mean deflected height estimated from 5 individual wave cycles from the digital imaging.

Table 1
Experimental values of $\frac{l_e}{l}$ in combined wave–current conditions.

Blade dimension markers		$l = 5$ cm, $d = 100$ μm ▲ ●	$l = 10$ cm, $d = 100$ μm ▲ ●	$l = 10$ cm, $d = 250$ μm ▲ ●	$l = 15$ cm, $d = 250$ μm ▲ ●
U_w, cm/s	U_c, cm/s	Effective length ratio from force measurements, l_e/l			
	0	0.29 ± 0.04	0.16 ± 0.03	0.34 ± 0.05	0.28 ± 0.04
	2.0	0.27 ± 0.04	0.15 ± 0.02	0.33 ± 0.04	0.26 ± 0.03
7.8	4.0	0.26 ± 0.04	0.12 ± 0.02	0.30 ± 0.04	0.22 ± 0.03
	6.0	0.19 ± 0.03	0.10 ± 0.01	0.24 ± 0.03	0.19 ± 0.02
	8.0	0.16 ± 0.02	0.08 ± 0.01	0.20 ± 0.03	0.18 ± 0.02
	10.0	0.14 ± 0.02	0.07 ± 0.01	0.19 ± 0.03	0.15 ± 0.02
	0	0.26 ± 0.03	0.11 ± 0.02	0.32 ± 0.04	0.20 ± 0.02
	2.0	0.24 ± 0.03	0.13 ± 0.02	0.30 ± 0.04	0.19 ± 0.02
11.0	4.0	0.24 ± 0.03	0.13 ± 0.02	0.28 ± 0.04	0.18 ± 0.02
	6.0	0.20 ± 0.02	0.11 ± 0.01	0.24 ± 0.03	0.13 ± 0.02
	8.0	0.14 ± 0.02	0.10 ± 0.01	0.19 ± 0.03	0.12 ± 0.01
	10.0	0.12 ± 0.02	0.08 ± 0.01	0.17 ± 0.02	0.12 ± 0.01

geometry (see figure caption) and wave velocity ($U_w = 11$ cm/s and 7.8 cm/s). For each blade-wave combination, the current velocity was varied from $U_c = 0$ to 30 cm/s. Importantly, these conditions all fall in the range of short waves, specifically, $L > 1$. For reference, the proposed limits of $U_c = \frac{1}{4}U_w$ and $U_c = 2U_w$ are indicated in Fig. 8 with red vertical lines. For $U_c < \frac{1}{4}U_w$, the measured and simulated effective lengths converged with the wave-only scaling (Eq. (9), shown with thin horizontal line in Fig. 8), with deviations of less than 15%. For $U_c > 2U_w$, l_e/l converged with the current-only scaling (Eq. (6), shown with thin black curve in Fig. 8), with deviations less than 5%. These two observations confirmed the limits defined in Section 2 for wave-dominated and current-dominated behavior. In between these limits, l_e/l had good agreement with the new wave–current formula, Eq. (13), shown with heavy black curve in Fig. 8, with deviations of less than 16%. Note, the current-dominated and combined wave–current models converged when $U_c/U_w > 2$. Finally, the new, wave–current formula (Eq. (13), heavy black curve in Fig. 8) provided a reasonable prediction for all U_c/U_w values, with a maximum deviation 20%, showing that the new predictor smoothly captures the full range of current to wave ratios.

5.4. Long waves without current, $L \ll 1$

For long waves (large wave excursion A_w) or short blades (small l), the ratio of blade length to wave excursion is small ($L = l/A_w \ll 1$), and the blade cannot follow the fluid motion during the entire wave cycle. Instead, the blade remains pronated but nearly stationary during a large fraction of the wave period. For simplicity, these were called long-wave conditions. For long-wave conditions, we hypothesized that the effective blade length could be described by the unidirectional current model (Eq. (6)), using the equivalent mean velocity $\sqrt{1/2}\,U_w$. Specifically, we hypothesized that for

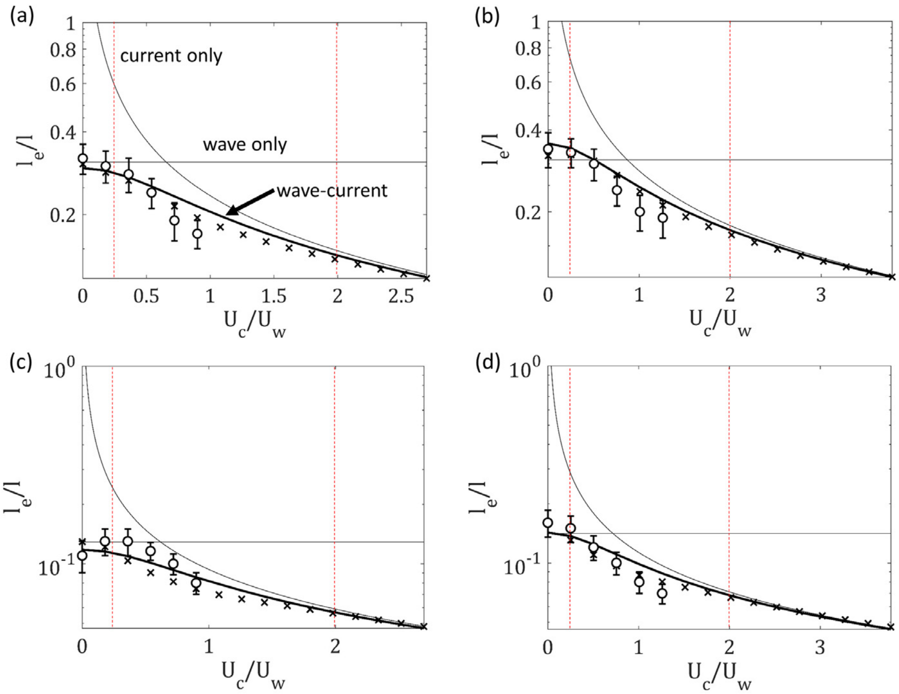

Fig. 8. Effective blade length normalized by full blade length, l_e/l, versus velocity ratio, U_c/U_w. Circles (o) denote measured values, and crosses (x) denote simulated values. The proposed wave–current model described by Eq. (13) is shown with a heavy black curve and labeled in sub-plot (a). The thin horizontal line denotes the wave-only scaling law, Eq. (9). The thin black curve denotes the current-only scaling law, Eq. (6). The vertical red lines denote the expected thresholds for wave-dominated ($U_c/U_w < \frac{1}{4}$), and current-dominated ($U_c/U_w > 2$) conditions. Blade geometry and wave conditions in each subplot: (a) $l = 10$ cm, $d = 250$ μm, $b = 1$ cm, $U_w = 11$ cm/s (b) $l = 10$ cm, $d = 250$ μm, $b = 1$ cm, $U_w = 7.8$ cm/s (c) $l = 10$ cm, $d = 100$ μm, $b = 1$ cm, $U_w = 11$ cm/s (d) $l = 10$ cm, $d = 100$ μm, $b = 1$ cm, $U_w = 7.8$ cm/s.

$L \ll 1$, $l_e/l = 1.1Ca_w^{-1/3}$ (Eq. (10)). Because this wave condition was outside the operating capabilities of the water channel, the proposed model was evaluated using the simulation. The simulated blade length and thickness were $l = 10$ cm and $d = 100$ μm, respectively. The wave amplitude was $a_w = 1.5$ cm, and the wave period was varied from $T = 1$ to 100 s, yielding L from 0.071 to 12, which spanned the long- and short-wave regimes, $L \ll$ and $\gg 1$, respectively. The simulated effective blade lengths were compared to the predicted effective blade length by considering the ratio of predicted l_e to simulated l_e (Fig. 9). For triangles (Δ), predicted l_e was calculated from the hypothesized long-wave equation (Eq. (10)). For crosses (x), predicted l_e was calculated from the short-wave equation (Eq. (9)). Fig. 9 shows that for $L < 1$ (long waves, or short blades), the long-wave equation (triangles, Eq. (10)) gave a more accurate prediction of l_e, i.e. the ratio was close to 1 with a maximum deviation of 7%. For $L > 1$ (short waves or long blades), the short-wave equation (crosses, Eq. (9)) gave a more accurate prediction of l_e, i.e. the ratio was close to 1 with a maximum deviation of 15%. This comparison confirmed the hypothesized long-wave equation (Eq. (10)) for $L < 1$. Between $L = 1$ and 5, both equations did well, and for $L > 5$ only the short-wave equation (Eq. (9)) provided a good prediction.

Summary

Luhar and Nepf (2011, 2016) previously defined the effective blade length, l_e, to characterize the impact of reconfiguration on the drag force experienced by an individual blade in unidirectional flow and in waves. The effective length is defined as the length of a rigid blade that experiences the same drag as a flexible blade of length l. This study proposed a new equation to predict the effective blade length in combined wave–current conditions. The new equation was confirmed using forces measured on flexible and rigid blades. In addition, a numerical model that simulated blade motion and forces on a flexible blade was validated using digital images of blade motion and the measured forces. Once validated, the numerical model was used to explore a wider parameter space than was available with the experimental facility. For a fixed wave condition, increasing current magnitude decreased both the mean deflected height and the range of blade motion. The mean deflected height had good agreement with the empirical equation for uni-directional current without waves (Luhar and Nepf, 2013), indicating that the presence of waves did not significantly impact the mean deflected height. The effective blade length was shown to be a function of both current and wave magnitude, and three regimes were identified for conditions with short waves ($L > 1$). For $U_c < 0.25U_w$, the blade motion was wave-dominated and the effective blade length was predicted by wave-only scaling (Eq. (9)). For $U_c > 2U_w$, the blade motion was current

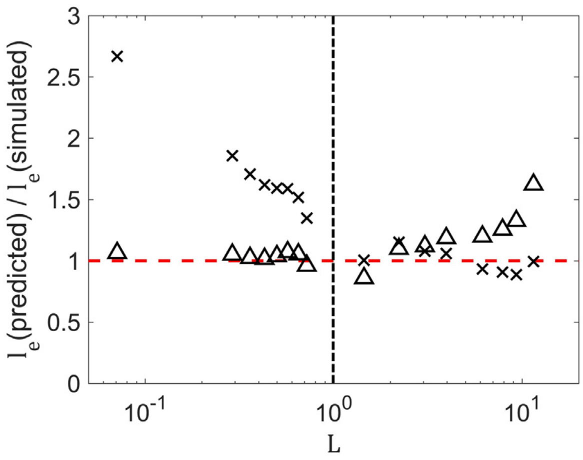

Fig. 9. Figure 9: Ratio of the effective blade length predicted from the two pure-wave scaling laws to the simulated effective blade length versus the blade length ratio $L = l/A_w$. For triangle (Δ) symbols the long-wave equation (Eq. (10)) was used to predict the effective blade length. For cross (x) the short-wave equation (Eq. (9)) was used to predict the effective blade length. The vertical dotted line denotes the threshold $L = 1$.

dominated, and the effective blade length was predicted from the current-only scaling (Eq. (6)). In between these limits, $0.25U_w < U_c < 2U_w$, the effective blade length was predicted by the new wave–current equation (Eq. (13)). Finally, the effective blade length for long waves, $L = l/A_w < 1$, was shown to follow the scaling for pure current, but using the equivalent mean velocity $\sqrt{1/2}\, U_w$.

Acknowledgment

This material is based upon work supported by the National Science Foundation, United States under grant EAR 1659923. Any opinions, findings, and conclusions or recommendations expressed in this material are those of the author(s) and do not necessarily reflect the views of the National Science Foundation. Data and MATLAB code are included in the PhD Thesis of Jiarui Lei, which will be available on MIT D-Space (https://dspace.mit.edu/), or may be obtained from Jiarui Lei.

Appendix A. Supplementary data

Supplementary material related to this article can be found online at https://doi.org/10.1016/j.jfluidstructs.2019.03.020.

References

Alben, S., Shelley, M., Zhang, J., 2002. Drag reduction through self-similar bending of a flexible body. Nature 420 (6915), 479. http://dx.doi.org/10.1038/nature01232.

Arkema, K., Griffin, R., Maldonado, S., Silver, J., Suckale, J., Guerry, A., 2017. Linking social, ecological, and physical science to advance natural and nature-based protection for coastal communities. Ann. New York Acad. Sci. http://dx.doi.org/10.1111/nyas.13322.

Augustin, L.N., Irish, J.L., Lynett, P., 2009. Laboratory and numerical studies of wave damping by emergent and near-emergent wetland vegetation. Coast. Eng. 56 (3), 332–340. http://dx.doi.org/10.1016/j.coastaleng.2008.09.004.

Barbier, E., Hacker, C., Kennedy, E., Koch, A., Stier, S., Silliman, B., 2011. The value of estuarine and coastal ecosystem services. Ecol. Monograph 81 (2), 169–193. http://dx.doi.org/10.1890/10-1510.1.

Bradley, K., Houser, C., 2009. Relative velocity of seagrass blades: Implications for wave attenuation in low-energy environments. JGR Earth Surf. 114 (F1), http://dx.doi.org/10.1029/2007JF000951.

Chandler, B.D., Hinwood, J.B., 1982. Combined wave–current forces on horizontal cylinders. In: Coastal Engineering 1982, pp. 2171–2188, http://dx.doi.org/10.1061/9780872623736.130.

Costanza, R., d'Arge, R., De Groot, R., Farber, S., Grasso, M., Hannon, B., Limburg, K., Naeem, S., O'neill, R.V., Paruelo, J., Raskin, R.G., 1997. The value of the world's ecosystem services and natural capital. Nature 387 (6630), 253–260. http://dx.doi.org/10.1038/387253a0.

Dalrymple, R., Kirby, J., Hwang, P., 1984. Wave diffraction due to areas of energy dissipation. J. Water. Port, Coastal, Ocean Eng. 110 (1), 67–79. http://dx.doi.org/10.1061/(ASCE)0733-950X(1984)110:1(67).

Ellington, C.P., 1991. Aerodynamics and the origin of insect flight. In: Adv. Insect Physiol., Vol. 23, Academic Press, pp. 171–210. http://dx.doi.org/10.1016/S0065-2806(08)60094-6.

Fornberg, B., 1998. Classroom note: Calculation of weights in finite difference formulas. SIAM Rev. 40 (3), 685–691.

Fourqurean, J.W., Duarte, C.M., Kennedy, H., Marbà, N., Holmer, M., Mateo, M.A., Apostolaki, E.T., Kendrick, G.A., Jenson, D.K., McGlathery, K.J., Serrano, O., 2012. Seagrass ecosystems as a globally significant carbon stock. Nat. Geosci. 5 (7), 505. http://dx.doi.org/10.1038/ngeo1477.

Goda, Y., Suzuki, Y., 1977. Estimation of incident and reflected waves in random wave experiments. In: Coastal Engineering 1976, pp. 828–845, http://dx.doi.org/10.1061/9780872620834.048.

Gosselin, F., de Langre, E., Machado-Almeida, B.A., 2010. Drag reduction of flexible plates by reconfiguration. J. Fluid Mech. 650, 319–341. http://dx.doi.org/10.1017/S0022112009993673.

Houser, C., Trimble, S., Morales, B., 2015. Influence of blade flexibility on the drag coefficient of aquatic vegetation. Estuar. Coasts 38 (2), 569–577. http://dx.doi.org/10.1007/s12237-014-9840-3.
Hu, Z., Suzuki, T., Zitman, T., Uittewaal, W., Stive, M., 2015. Laboratory study on wave dissipation by vegetation in combined current–wave flow. Coast. Eng. 88, 131–142. http://dx.doi.org/10.1016/j.coastaleng.2014.02.009.
Infantes, E., Orfila, A., Terrados, J., Luhar, M., Simarro, G., Nepf, H., 2012. Effect of a seagrass (*Posidonia oceanica*) meadow on wave propagation. Mar. Ecol. Prog. Ser. 456, 63–72. http://dx.doi.org/10.3354/meps09754.
Keulegan, G., Carpenter, L.H., 1958. Forces on cylinder and plates in an oscillating fluid. J. Res. Natl. Bur. Stand. 60 (5), 423–440. http://dx.doi.org/10.6028/jres.060.043.
Leclercq, T., de Langre, E., 2018. Reconfiguration of elastic blades in oscillatory flow. J. Fluid Mech. 838, 606–630. http://dx.doi.org/10.1017/jfm.2017.910.
Lei, J., Nepf, H., 2016. Impact of current speed on mass flux to a model flexible seagrass blade. J. Geophys. Res. 121 (7), 4763–4776. http://dx.doi.org/10.1002/2016JC011826.
Lei, J., Nepf, H., 2019. Wave damping by flexible vegetation: connecting individual blade dynamics to the meadow scale. Coast. Eng. 147, 138–148. http://dx.doi.org/10.1016/j.coastaleng.2019.01.008.
Li, C.W., Yan, K., 2007. Numerical investigation of wave–current–vegetation interaction. J. Hydraul. Eng. 133 (7), 794–803. http://dx.doi.org/10.1061/(ASCE)0733-9429(2007)133:7(794).
Losada, I.J., Maza, M., Lara, J.L., 2016. A new formulation for vegetation-induced damping under combined waves and currents. Coast. Eng. 107, 1–13. http://dx.doi.org/10.1016/j.coastaleng.2015.09.011.
Luhar, M., 2012. Analytical and Experimental Studies of Plant-Flow Interaction at Multiple Scales (Doctoral dissertation). Massachusetts Institute of Technology.
Luhar, M., Infantes, E., Nepf, H., 2017. Seagrass blade motion under waves and its impact on wave decay. JGR-Oceans 12, 2. http://dx.doi.org/10.1002/2017JC012731.
Luhar, M., Nepf, H., 2011. Flow induced reconfiguration of buoyant and flexible aquatic vegetation. Limnol. Oceanogr. 56 (6), 2003–2017. http://dx.doi.org/10.4319/lo.2011.56.6.2003.
Luhar, M., Nepf, H.M., 2013. From the blade scale to the reach scale: A characterization of aquatic vegetative drag. Adv. Water Resour. 51, 305–316. http://dx.doi.org/10.1016/j.advwatres.2012.02.002.
Luhar, M., Nepf, H., 2016. Wave-induced dynamics of flexible blades. J. Fluids Struct. 61, 20–41. http://dx.doi.org/10.1016/j.jfluidstructs.2015.11.007.
Mendez, F.J., Losada, I.J., 2004. An empirical model to estimate the propagation of random breaking and nonbreaking waves over vegetation fields. Coast. Eng. 51 (2), 103–118. http://dx.doi.org/10.1016/j.coastaleng.2003.11.003.
Mullarney, J., Henderson, S., 2010. Wave-forced motion of submerged single-stem vegetation. JGR-Oceans 115 (C12), http://dx.doi.org/10.1029/2010JC006448.
Paul, M., Amos, C.L., 2011. Spatial and seasonal variation in wave attenuation over zostera noltii. J. Geophys. Res. 116 (C8), http://dx.doi.org/10.1029/2010JC006797.
Paul, M., Bouma, T.J., Amos, C.L., 2012. Wave attenuation by submerged vegetation: combining the effect of organism traits and tidal current. Mar. Ecol. Prog. Ser. 444, 31–41. http://dx.doi.org/10.3354/meps09489.
Stratigaki, V., Manca, E., Prinos, P., Losada, I.J., Lara, J.L., Sclavo, M., Amos, C.L., Caceres, I., Sánchez-Arcilla, A., 2011. Large-scale experiments on wave propagation over *Posidonia oceanica*. J. Hydraul. Res. 49 (sup1), 31–43. http://dx.doi.org/10.1080/00221686.2011.583388.
Taylor, J., 1997. An Introduction To Error Analysis: The Study of Uncertainties in Physical Measurements, second ed. Oxford University Press.
Waycott, M., Longstaff, B.J., Mellors, J., 2005. Seagrass population dynamics and water quality in the Great Barrier Reef region: a review and future research directions. Mar. Pollut. Bull. 51 (1–4), 343–350. http://dx.doi.org/10.1016/j.marpolbul.2005.01.017.
Ysebaert, T., Yang, S.L., Zhang, L., He, Q., Bouma, T.J., Herman, P.M., 2011. Wave attenuation by two contrasting ecosystem engineering salt marsh macrophytes in the intertidal pioneer zone. Wetlands 31 (6), 1043–1054. http://dx.doi.org/10.1007/s13157-011-0240-1.
Zeller, R., Weitzman, J., Abbett, M., Zarama, F., Fringer, O., Koseff, J., 2014. Improved parameterization of seagrass blade dynamics and wave attenuation based on numerical and laboratory experiments. Limnol. Oceanogr. 59 (1), 251–266. http://dx.doi.org/10.4319/lo.2014.59.1.0251.